Quantitative assessment of tomographic proxies for lowermost mantle composition and mineralogy

Justin Leung[a], Andrew M. Walker[a], Paula Koelemeijer[a], Federica Restelli[b], D. Rhodri Davies[c]

[a]*Department of Earth Sciences, University of Oxford, South Parks Road, Oxford OX1 3AN, United Kingdom,*
[b]*Department of Earth Sciences, Queen's Building, Royal Holloway University of London, Egham Hill, Egham, Surrey TW20 0EX, United Kingdom,*
[c]*Research School of Earth Sciences, The Australian National University, Canberra, Australia,*

Abstract

Large low velocity provinces (LLVPs) dominate the lowermost mantle, but their detailed thermochemical nature remains a topic of discussion. Particularly, it is unclear to what extent the bridgmanite to post-perovskite phase transition is able to explain their velocity characteristics. Robust constraints on the origin of these seismic structures would shed light on large-scale dynamic processes in the mantle. Here, we examine the combined effects of both chemical heterogeneity and phase transitions on lowermost mantle tomographic signatures. We calculate synthetic seismic velocities expected from a range of scenarios for the stability of post-perovskite within models of different lowermost mantle temperatures and compositions using recent thermodynamic data. These are filtered to account for the limited resolution of seismic tomography. We are able to quantitatively compare our synthetic velocities with a recent Backus-Gilbert based tomography model. Crucially, this model provides robust ratios and correlations of velocity anomalies derived from nearly identical V_p and V_s resolution, and includes uncertainty quantification that accounts for both data and theoretical errors. By rejecting synthetic models that do not fit within tomographic uncertainties, we quantitatively show the following: (i) the root mean square of velocity anomalies cannot be entirely explained by LLVPs with a primordial composition; and (ii) elevated $R_{s/p}$ $(= d\ln V_s/d\ln V_p)$ and negative correlation between shear-wave and bulk-sound velocity ($r_{s\text{–}c}$) in the lowermost mantle cannot be explained by thermochemical LLVPs alone, but require bridgmanite and post-perovskite to co-occur at depth in the mantle. These seismological observables thus do not provide useful information about chemical heterogeneity in the deep mantle.

Keywords: LLVPs, Post-perovskite, SOLA, Lowermost mantle composition, Uncertainties, Seismic tomography

---

1. Introduction

Large low velocity provinces (LLVPs) are two seismically slower structures lying in the lowermost mantle beneath the Pacific and Africa, spanning 25 % of the core-mantle boundary (CMB) with estimated negative S-wave velocity anomalies of 1.5-5% (Cottaar and Lekic, 2016; McNamara, 2019). Because of their size, LLVPs have large influences on planetary scale dynamics, such as the influence of density variations on the global mantle flow, which also results in dynamic topography of the surface and CMB (Hager et al., 1985; Garnero et al., 2016; Richards et al., 2023; Davies et al., 2023). Therefore, understanding the origin and thermochemical structure of these deep mantle features provides a way to better interpretation of the coupling between the outer core and the mantle, which links to heat flux from the core (McNamara, 2019; Schuberth et al., 2009a), geomagnetic reversals (Tarduno et al., 2015), and the generation and stability of mantle plumes (Burke et al., 2008; Tarduno et al., 2015; Thorne et al., 2004). However, because of the non-linear sensitivity of seismic wave speeds to pressure, temperature, composition and mineral phases, the composition and origin of LLVPs are still contested, particularly focusing on the extent to which they are thermochemical.

Lowermost mantle tomographic signatures include the observed anti-correlation between $d \ln V_s$ and $d \ln V_c$ (hereon referred to as $r_{s\text{–}c}$) and the elevated ratio ($R_{s/p} = d \ln V_s / d \ln V_p$) between 2.6 and 3.4 (Masters et al., 2000; Moulik and Ekström, 2016; Ritsema and Van Heijst, 2002; Su and Dziewonski, 1997). Both the bulk and shear moduli soften with increasing temperature, therefore $r_{s\text{–}c}$ stays strongly positive and $R_{s/p}$ remains below 2.5 for pure temperature variations (in the absence of temperature-dependent phase transitions, Karato and Karki, 2001). Because $r_{s\text{–}c}$ and $R_{s/p}$ cannot be explained by thermal effects alone, they have been interpreted as evidence for LLVPs of thermochemical origin. This interpretation has been supported by other geophysical and geochemical observations, including the correlation of LLVP edges with hotspots containing enriched isotope signatures, steep V_s gradients of 1.3—6 %/100 km (Ni et al., 2002), and anti-correlations between V_s and density inside (and outside) LLVPs (Ishii and Tromp, 1999; Trampert et al., 2004). However, studies have suggested the possibility of thermal diffusion to explain the velocity gradients at the LLVP margins by geodynamic models with substantial CMB heat flux (e.g. Schuberth et al., 2009b), and recent observations of lower V_s gradients at the edges of LLVPs (Ward et al., 2020). Additionally, resolving lowermost mantle density from seismic and geodetic data remains debatable due to limited data and its correlations with V_p, V_s (Akbarashrafi et al., 2018; Robson et al., 2021) and viscosity (Forte et al., 2015) in data. Even if LLVPs were to be thermochemical, multiple compositions can explain the characteristics of these observed anomalies. The first is the preservation of primordial mantle material segregated during top-down crystallisation of a basal magma ocean (BMO, Labrosse et al., 2007), which is enriched with iron-rich melts generated in the primordial mantle transition zone (Lee et al., 2010). A second proposed composition is that LLVPs are made of subducted iron- and silicon-rich Hadean crust along with a terrestrial regolith comprising chondritic and solar-wind-implanted material (Tolstikhin and Hofmann, 2005). These first two scenarios suggest that LLVPs are formed of primordial material, and thus imply that they are stable, longlived structures throughout Earth's evolution. Alternatively, LLVPs could be piles of accumulated recycled oceanic crust from subducted slabs (Niu, 2018), which are denser than the background mantle at lowermost mantle pressures (Hirose et al., 2005). This implies that LLVPs are metastable features with material constantly being added and removed, and therefore would have less well defined margins (Jones et al., 2020).

Yet, numerous studies (e.g. Davies et al., 2012; Schuberth et al., 2009b) have suggested that elevated ratios and anti-correlations in the lowermost mantle do not require compositional heterogeneity. They favour an alternative explanation due to the bridgmanite-post-perovskite (bdg-pPv) phase transition, which experimental results suggest happen at 200-300 km above the CMB (Murakami et al., 2004). The phase transition exhibits a 1-4% increase in V_s, a small change in V_p and a decrease in V_c, which results in a higher $R_{s/p}$ and a negative r_{s-c} (Cobden et al., 2015; Oganov and Ono, 2004; Tsuchiya et al., 2004). The large Clapeyron slope of the bdg-pPv phase transition, as well as the proposed 3-4 order-of-magnitude-decrease in viscosity of post-perovskite relative to bridgmanite, is thought to destabilise the thermal boundary layer above the CMB and promote plume formation (Ammann et al., 2010; Hirose, 2006). LLVPs of thermal origin have been suggested as plumes focused into clusters by adjacent regions dominated by subduction (Davies et al., 2012; McNamara, 2019; Schubert et al., 2004). Nonetheless, large uncertainties in mineral physics at lowermost mantle temperature and pressure conditions indicate that the phase transition is still poorly understood (Cobden et al., 2015). Additionally, the composition of bridgmanite and post-perovskite, poorly constrained in the lowermost mantle, affect both the phase transition pressure (hence depth) and two-phase region. In particular, the incorporation of iron increases the thickness of the two-phase region and decreases the pressure at which the phase boundary occurs (Catalli et al., 2009).

Previous studies (e.g. Davies et al., 2012; Koelemeijer et al., 2018) have conducted synthetic-tomographic comparisons to determine whether compositional heterogeneity (chemical) or phase transitions (mineralogical) better explain lowermost mantle seismic signatures. However, Davies et al. (2012) only investigate models where post-perovskite is always present, and therefore are limited by scenarios where both chemical and mineralogical effects are important. Koelemeijer et al. (2018) investigates both, but different post-perovskite scenarios are artificially created, and only pyrolite and basaltic LLVP compositions are considered. Additionally, the tomography model used in these studies only have similar, but not identical resolution for $d \ln V_s$ and $d \ln V_p$, which is important for obtaining robust velocity ratios and correlations. In this study, we therefore consistently examine the combined effects of LLVP composition and the bdg-pPv phase transition on lowermost mantle seismic velocity anomalies, ratios and correlations. We expand on the study of Koelemeijer et al. (2018) by examining more different LLVP compositions, utilising up-to-date and self-consistent thermodynamic parameters, and using a tomographic model with nearly equal resolution on $d \ln V_s$ and $d \ln V_p$ that includes uncertainty quantification. This enables us to quantitatively assess our LLVP compositions and post-perovskite stability scenarios by eliminating synthetic velocity models that fall outside of tomographic uncertainties.

2. Methods

To address the relative effects of composition and mineralogy on seismic signatures in the lowermost mantle, we compare observations from seismic tomography (Restelli et al., 2023) with synthetic seismic velocity models of various LLVP composition and post-perovskite stability scenarios (Fig. 1). To generate these synthetic models, we utilise realistic temperature and compositional fields from a geodynamic modelling study (Davies et al., 2012, section 2.1). We calculate the equilibrium phase assemblages for a range of LLVP compositions and post-perovskite stability scenarios (section 2.2). By combining the temperature field and equilibrium phase assemblages, we calculate synthetic velocity models, which are filtered to account for the limited resolution of the observation-based seismic tomography model (section 2.3). Only after filtering can we quantitatively compare the predicted seismic velocity models with tomographic observations, where we reject synthetic velocity models that fall outside of the available tomographic uncertainties (section 2.4).

2.1. Geodynamic model

We use high-resolution global mantle circulation models from Davies et al. (2012), which were originally designed to investigate the origin of LLVPs. These models were based on a modified version of TERRA (Davies et al., 2013), a finite-element mantle convection code that solves the conservation equations of mass, momentum and energy at infinite Prandtl number (Stokes flow) in a spherical shell. A mesh of 80 million grid points ($\sim$25 km grid cells) enabled the simulation to model Earth-like mantle convection at a high

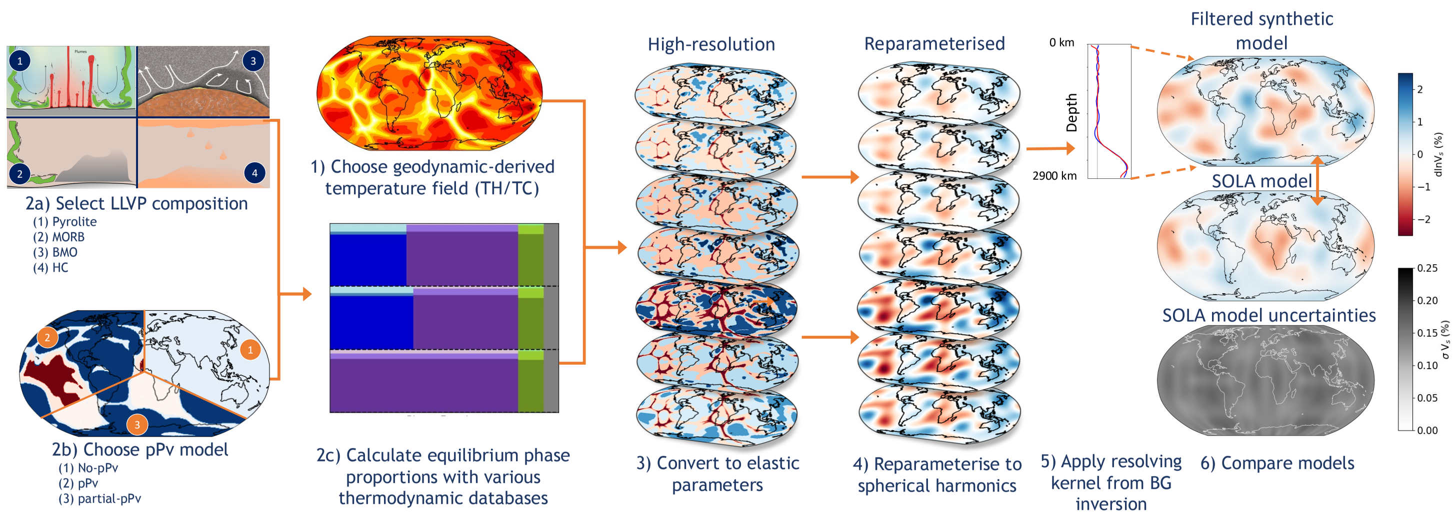

Figure 1: A schematic of the workflow to generate and compare synthetic velocity models with tomographic results. Each step is expanded on in the text. MORB = Mid-ocean ridge basalt, BMO = Basal magma ocean, HC = Hadean (early Earth) crust, pPv = post-perovskite, SOLA Model = Subtractive Optimally Localised Zverages tomographic model, referring to the model from Restelli et al. (2023).

Rayleigh Number ($Ra \approx 5 \times 10^8$ Pa s). The models incorporated compressibility, in the form of the anelastic liquid approximation. The viscosity profile was temperature and depth dependent, and included changes to account for the dynamic effects of the 410 and 660-km discontinuities. However, the dynamic effects of the post-perovskite phase transition were not considered. These models were bounded by isothermal boundary conditions of 300 K at the surface and 4000 K at the CMB. A free-slip boundary condition was imposed at the CMB, while surface motion was governed by a plate model with 300 Myr of plate motion history (Stampfli and Borel, 2002; Stampfli and Hochard, 2009). The imposed plate motion captured the effects of surface-plate strength and plate-boundary weakness on convection, and improved spatio-temporal constraints on long-wavelength mantle structures, allowing for predictions of the mantle's thermal structure in space and time. Models included a compositional field (X) simulated by the ratio tracer particle method, with $\approx 2.0 \times 10^9$ active tracers of two distinct types (dense material, $X = 1$; regular material, $X = 0$). Altogether, the simulation of Earth-like mantle convection, multi-parameter dependent viscosity profiles, boundary conditions governed by 300 Myr of plate motion, and particle tracing of compositional heterogeneity enabled this suite of models to generate synthetic mantle structures with a comparable distribution of heterogeneity as observed seismically. This is evidenced by their comparison with numerous seismic tomographic models (e.g. S40RTS (Ritsema et al., 2011), SP12RTS (Koelemeijer et al., 2016)) via several tomographic-geodynamic comparison studies (e.g. Davies et al., 2015; Koelemeijer et al., 2018; Trautner et al., 2023).

We utilise the temperature and compositional outputs of the geodynamic models as inputs for our synthetic velocity model calculations. We use two temperature fields from Davies et al. (2012): (i) a purely thermal (TH) model without any chemical heterogeneity; and (ii) a thermochemical (TC) model, with chemically distinct, denser material (2.75 % higher intrinsic density) resembling large-scale piles in the lowermost mantle. Similar to Davies et al. (2012) and Koelemeijer et al. (2018), the availability of different temperature fields for a thermal and thermochemical mantle enables us to compare our suite of LLVP composition models in a self-consistent manner. The compositional field (X) represents the fraction of chemically distinct material within a grid cell. In our thermochemical models, we define LLVPs to be at locations where $X \geq 0.6$. We find that the choice of this compositional threshold has no major effect on the spatial definition of the LLVPs as changes in X from 0 to 1 occur over short distances, due to the fact that chemical diffusivity is negligible.

2.2. Calculating equilibrium phase assemblages

To calculate the equilibrium phase assemblages for our synthetic models, we utilise a "constrained free energy minimisation" algorithm in Burnman (Myhill et al., 2023). Rather than solving the full Gibbs Energy minimalisation problem for all known phases, this solver optimises equilibrium relations for fixed assemblages. The fixed assemblages are pre-determined from known major phase assemblages for the various LLVP compositions (Irifune and Tsuchiya, 2015; Stixrude and Lithgow-Bertelloni, 2011, 2021). Because the major mineral phases in the lowermost mantle are relatively well-known and thought to remain relatively constant throughout lowermost mantle pressures and temperatures for a given composition, the Burnman solver outputs identical results to a full Gibbs Energy minimiser (e.g. HeFESTo, Stixrude and Lithgow-Bertelloni, 2021). Thus, by avoiding the full Gibbs Energy minimisation, the Burnman solver calculates equilibrium phase assemblages with a substantially lower computational cost. For the calculation, we utilise up-to-date thermodynamic parameters from the SLB2022 (Stixrude and Lithgow-Bertelloni, 2021) mineralogical model, which includes improved calculations for the pressure dependence of non-ideal solution parameters such as the bulk modulus. To perform this energy minimisation calculation, four pieces of information are needed: (i) temperature; (ii) pressure (depth); (iii) oxide composition, here represented with 6 components; and (iv) constraints on post-perovskite stability regions. The fixed mineral assemblage as input for the energy minimisation is determined by the post-perovskite stability and 6-oxide-component composition (detailed in Table S1). The temperature field is obtained from the geodynamic model (see above), and the pressure field is converted from the depth layers in the geodynamic model of Davies et al. (2012) using PREM (Dziewonski and Anderson, 1981).

We fix the ambient mantle to have a pyrolite composition, only varying the composition of the LLVPs between the different synthetic velocity models. We examine four different LLVP compositions (Table S1), each representing a proposed origin (see the Introduction). We first consider LLVPs as purely thermal features, where LLVPs have a pyrolite composition. To be self-consistent with the geodynamic simulation, we use the TH temperature model for this LLVP composition (black line in Fig. 2a). We use the TC temperature model (black line in Fig. 2b) for the other three LLVP compositions: recycled oceanic crust (MORB), remnants of basal magma ocean (BMO), and Hadean crust (HC). We therefore extend the study of Koelemeijer et al. (2018), who only considered one basaltic thermochemical composition. For each LLVP composition, we specify a mineral assemblage from the SLB2022 mineralogical database (Stixrude and Lithgow-Bertelloni, 2021) as input for the energy minimisation (see supplementary material).

The ambiguity of the bridgmanite-post-perovskite (bdg-pPv) phase boundary is due to large uncertainties in lowermost mantle temperatures, pressures and compositions, such that we expect the phase boundary to be different for each of the LLVP compositions described above. To address this ambiguity, we implement three different post-perovskite stability scenarios per LLVP composition. The first scenario inhibits any existence of post-perovskite in the lowermost mantle, representing a phase boundary that occurs at temperatures and pressures higher than the CMB (hereon termed the "no-pPv" scenario). The second scenario allows post-perovskite to be stable in the lowermost mantle (hereon termed the "pPv" scenario) at P-T conditions determined by the thermodynamic mineralogical model (Fig. 2). The third scenario is a mixture of the first two, with post-perovskite restricted to occur solely outside of LLVPs (hereon termed the "partial-pPv" scenario). We include this scenario because the post-perovskite phase transition has a positive Clapeyron slope, making it less likely for post-perovskite to occur in LLVPs as they are thought to be warmer than the surrounding mantle. This is supported by observations of post-perovskite detected mostly in the colder regions of the lowermost mantle (Cobden et al., 2015). We implement these three post-perovskite scenarios with a thermodynamically self-consistent ap-

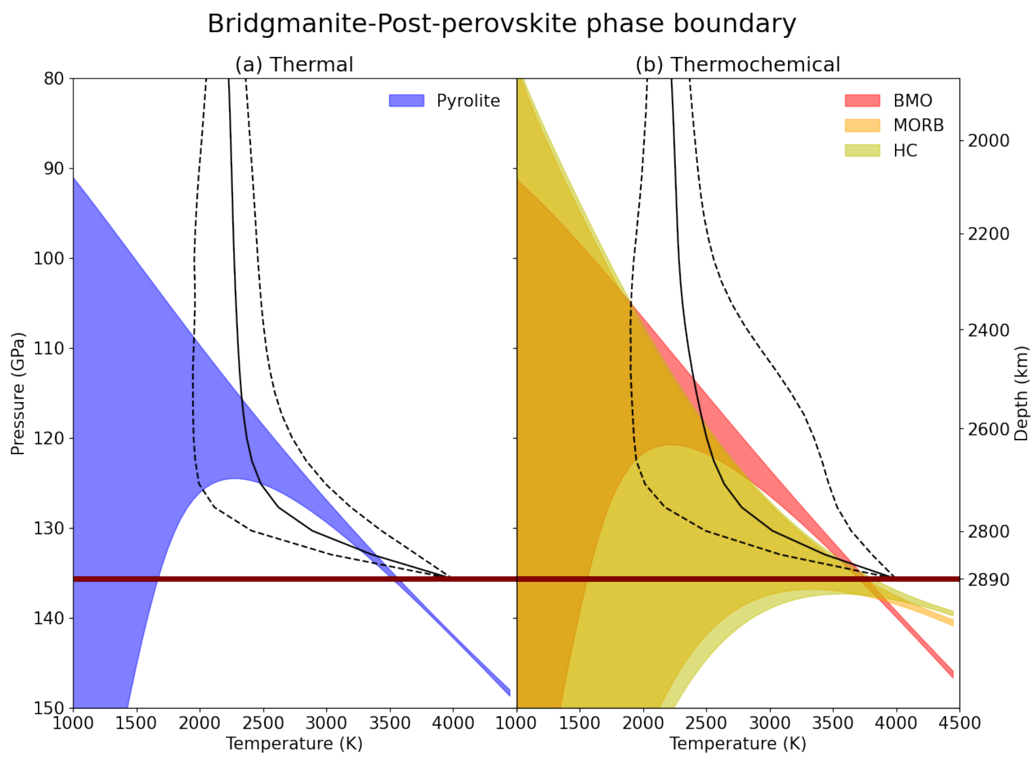

Figure 2: The bridgmanite post-perovskite phase transition calculated using the SLB2022 mineralogical model for the different (a) thermal (TH) and (b) thermochemical (TC) LLVP compositions. The shaded areas in both plots represent the two-phase region, which is the pressure and temperature conditions where both bridgmanite and post-perovskite occur. The solid and two dashed black lines show the mean, 10, and 90 percentile temperature respectively for the (a) TH and (b) TC model of Davies et al. (2012). The horizontal maroon line indicates the CMB pressure. MORB = Mid-ocean ridge basalt, BMO = Basal magma ocean, HC = Hadean (early Earth) crust.

proach by directly including or omitting the post-perovskite phase in the fixed assemblage before optimising for equilibrium phase proportions in Burnman. This is an improvement compared to Koelemeijer et al. (2018), who artificially shifted the bdg-pPv phase boundary to consider different post-perovskite stability scenarios.

2.3. Tomographic observations

We compare our synthetic velocity models with tomographic observations from Restelli et al. (2023), derived using the Subtractive Optimally Localised Averages (SOLA) method. The SOLA method is a variant of Backus-Gilbert inverse theory that calculates some optimally-localised average ($\hat{m}$) over the "true" model m^t (Zaroli, 2016). The averaging process removes the non-uniqueness in the solution, such that additional regularisation terms (e.g. model smoothness) are not needed to constrain the solution. The average can be expressed as

$$\hat{m} = \int \hat{R} m^t + \text{(propagated noise)}, \tag{1}$$

where $\hat{R}$ is the resolving kernel that is optimised to match a pre-defined target kernel (Restelli et al., 2023; Zaroli, 2016). The advantage of optimising for a resolving kernel is to provide direct control of the local model resolution, which here provided equal resolution on both $d\ln V_p$ and $d\ln V_s$. Therefore, we can calculate robust values of ratios and correlations between $d\ln V_s$ and $d\ln V_p$, and consequently also $d\ln V_c$, given that the SOLA-derived averages refer to the same region inside the Earth. Other tomographic models can only ensure similar but not equal resolution for $d\ln V_s$ and $d\ln V_p$, such that ratios and correlations of velocity anomalies may include inversion artefacts (e.g. Koelemeijer et al., 2018). Another benefit of this method is the availability of a quantified tomographic uncertainty that trades off with resolution. This uncertainty can be used as a concrete constraint, allowing us to quantitatively rule out synthetic velocity models that are outside of the uncertainty range. This provides a rigorous method to compare geodynamic and tomographic models, in contrast to previous studies (e.g. Koelemeijer et al., 2018; Schuberth et al., 2009b) that were only able to assess the relative fit of their synthetic models.

The tomographic results of Restelli et al. (2023) were obtained from the splitting functions of 143 spheroidal normal modes that are sensitive to the crust and the mantle. The model was laterally parameterised in spherical harmonics of even degrees up to degree 8, such that 1-D inversions with uncertainty bounds could be conducted independently for each spherical harmonic coefficient. The uncertainties encompassed both data and theoretical errors, with a factor of 2 applied to the data uncertainties to account for theoretical errors due to the use of the self-coupling approximation. Additionally, Restelli et al. (2023) included the simultaneous sensitivity of normal modes to multiple physical parameters (e.g. v_p and ρ) as additional 3-D noise (Masters and Gubbins, 2003), such that the effects of unmodelled model parameters are captured in the uncertainties. The final model consists of four layers of averaged velocities, with the lowest layer having particular sensitivity to the lowermost mantle between depths of 2100 km and 2890 km (CMB). We use the velocities in this layer to compare with our synthetic velocity models (Fig. 3).

To quantitatively compare our synthetic velocity models with the tomography model, we apply the resolving kernel to our synthetic models. The resolving kernel accounts for the difference in resolution between the geodynamic model (e.g. $\sim$25 km) and the tomographic model (e.g. $\sim$5000 km wavelength for spherical harmonic degree 8), thus it is synonymous with

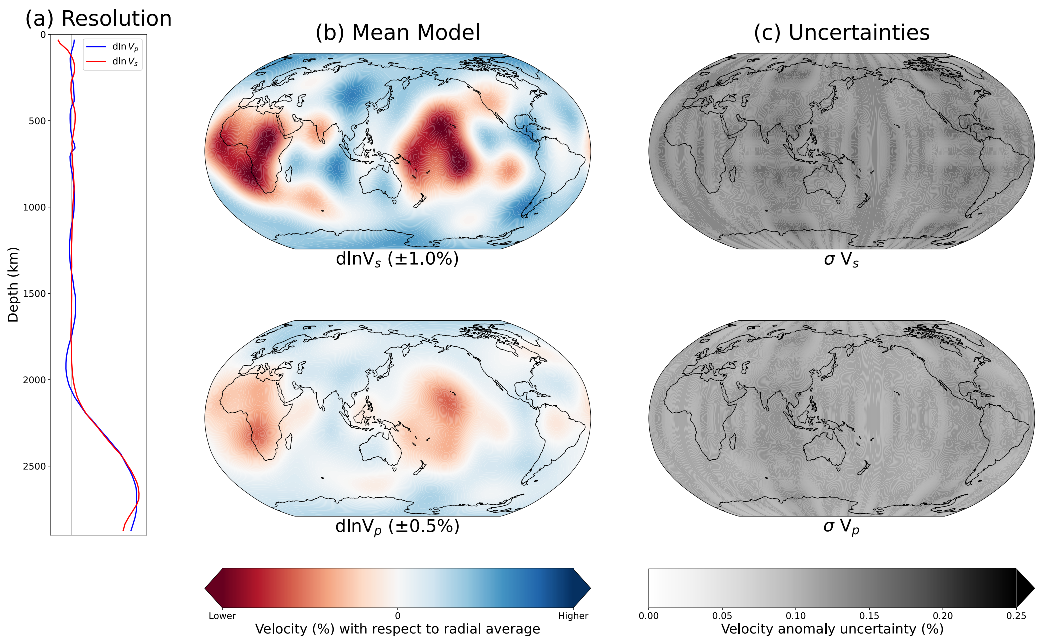

Figure 3: A plot summarising the tomographic model of Restelli et al. (2023) in the deep mantle. a) The equal resolving kernel for $d \ln V_p$ (blue) and $d \ln V_s$ (red). Mean amplitudes (b) and uncertainties (c, 1σ) are shown for $d \ln V_p$ (top) and $d \ln V_s$ (bottom). The maximum of the scale for $d \ln V_s$ ($\pm 1.0\%$) is twice that of $d \ln V_p$ ($\pm 0.5\%$), so that the two plots have similar colour intensity and patterns for $R_{s/p} = 2$.

the tomographic resolution operator available for other tomographic models (e.g. S40RTS (Ritsema et al., 2011), SP12RTS (Koelemeijer et al., 2016)). The resolving kernel condenses the synthetic velocity models into a weighted depth average that can be directly and quantitatively compared with the tomographic observations.

2.4. Calculation of quantitative metrics

Both the synthetic seismic velocities and the observed tomography are parameterised in the spherical harmonic basis. To evaluate their amplitudes, we compute the root mean square (RMS) of shear-wave velocity anomalies ($d\ln V_s$) and compressional-wave velocity anomalies ($d\ln V_p$) as:

$$d\ln V_s = \sqrt{\frac{\sum_{l=0}^{\infty}\sum_{m=-l}^{l} f_{lm}^2}{4\pi}}, \tag{2}$$

$$d\ln V_p = \sqrt{\frac{\sum_{l=0}^{\infty}\sum_{m=-l}^{l} g_{lm}^2}{4\pi}}, \tag{3}$$

with f_{lm} and g_{lm} representing the spherical harmonic coefficients for $d\ln V_s$ and $d\ln V_p$ respectively at degree l and order m. Similar to Koelemeijer et al. (2018), the $d\ln V_s/d\ln V_p$ ratio ($R_{s/p}$) is taken by dividing the RMS values of $d\ln V_s$ and $d\ln V_p$:

$$R_{s/p} = \sqrt{\frac{\sum_{l=0}^{\infty}\sum_{m=-l}^{l} f_{lm}^2}{\sum_{l=0}^{\infty}\sum_{m=-l}^{l} g_{lm}^2}}. \tag{4}$$

The bulk sound velocity anomaly at depth d is calculated by (Masters et al., 2000):

$$d\ln V_c(d) = \frac{d\ln V_p(d) - \gamma(d)\times d\ln V_s}{1-\gamma(d)} \tag{5}$$

where $\gamma(d) = \frac{4}{3}\frac{v_s^2(d)}{v_p^2(d)}$, and V_s and V_p are the radially averaged shear-wave and compressional-wave velocities from PREM (Dziewonski and Anderson, 1981) at depth d. The $d\ln V_s$-$d\ln V_c$ correlation (r_{s-c}) is then calculated by:

$$r_{s-c} = \frac{\sum_{l=0}^{\infty}\sum_{m=-l}^{l} f_{lm}h_{lm}}{\sqrt{\sum_{l=0}^{\infty}\sum_{m=-l}^{l} f_{lm}^2 \times \sum_{l=0}^{\infty}\sum_{m=-l}^{l} h_{lm}^2}}, \tag{6}$$

with h_{lm} representing the spherical harmonic coefficients for $d\ln V_c$ at degree l and order m.

To obtain uncertainties for the RMS $d\ln V_s$, RMS $d\ln V_p$, $R_{s/p}$ and r_{s-c}, we treat each of the spherical harmonic coefficients as Gaussian variables (with the associated uncertainty as the standard deviation) and conduct 1,000,000 realisations (drawing each time a sample for each coefficient) to obtain distributions for each of the seismic characteristics listed above. For each of the four distributions, we then obtain the median, 1σ (68%) uncertainty range and 2σ (95.4%) uncertainty range. We subsequently reject synthetic models that do not fit within the 2σ uncertainty range of either both observed RMS velocities, or both the observed $R_{s/p}$ and $r_{s\text{–}c}$.

3. Results

3.1. Amplitudes of velocity anomalies

All of the synthetic velocity models generate degree-2 structures that resemble tomographic observations: the two LLVPs beneath Africa and the Pacific, surrounded by fast anomalies (Fig 4 and S1). The Pacific slow anomaly appears to be shifted eastward compared to its location in the tomography model of Restelli et al. (2023), which is likely due to uncertainties around the plate reconstructions and reference frame. Within the LLVPs, the $d \ln V_s$ amplitudes of the synthetic velocity models fall within the range of 1.5-5% (the range of seismic tomography models summarised by McNamara (2019)). However, the amplitudes are considerably higher in iron-rich LLVP compositions (BMO and HC) compared to the tomographic model of Restelli et al. (2023), as suggested in previous studies (e.g. Davies et al., 2012). This is because the higher iron content and temperature both decrease V_s to generate larger velocity variations.

To quantitatively assess the amplitudes, we compare the RMS velocities of the different filtered synthetic velocity models with tomographic observations (Fig. 5). We see that the amplitudes of velocity anomalies are more affected by LLVP composition than the presence of post-perovskite. The RMS for $d \ln V_s$ (Fig. 5b) in models without post-perovskite and with post-perovskite of the same composition (same colour, different symbols) differ by no more than 0.4 %, whereas the velocity amplitudes can differ up to 0.8 % between models of different LLVP compositions (same symbol, different colours). The results of RMS for $d \ln V_p$ (Fig. 5a) show a fit to both pyrolite (blue) and MORB (orange) LLVP composition. Both pyrolite and MORB

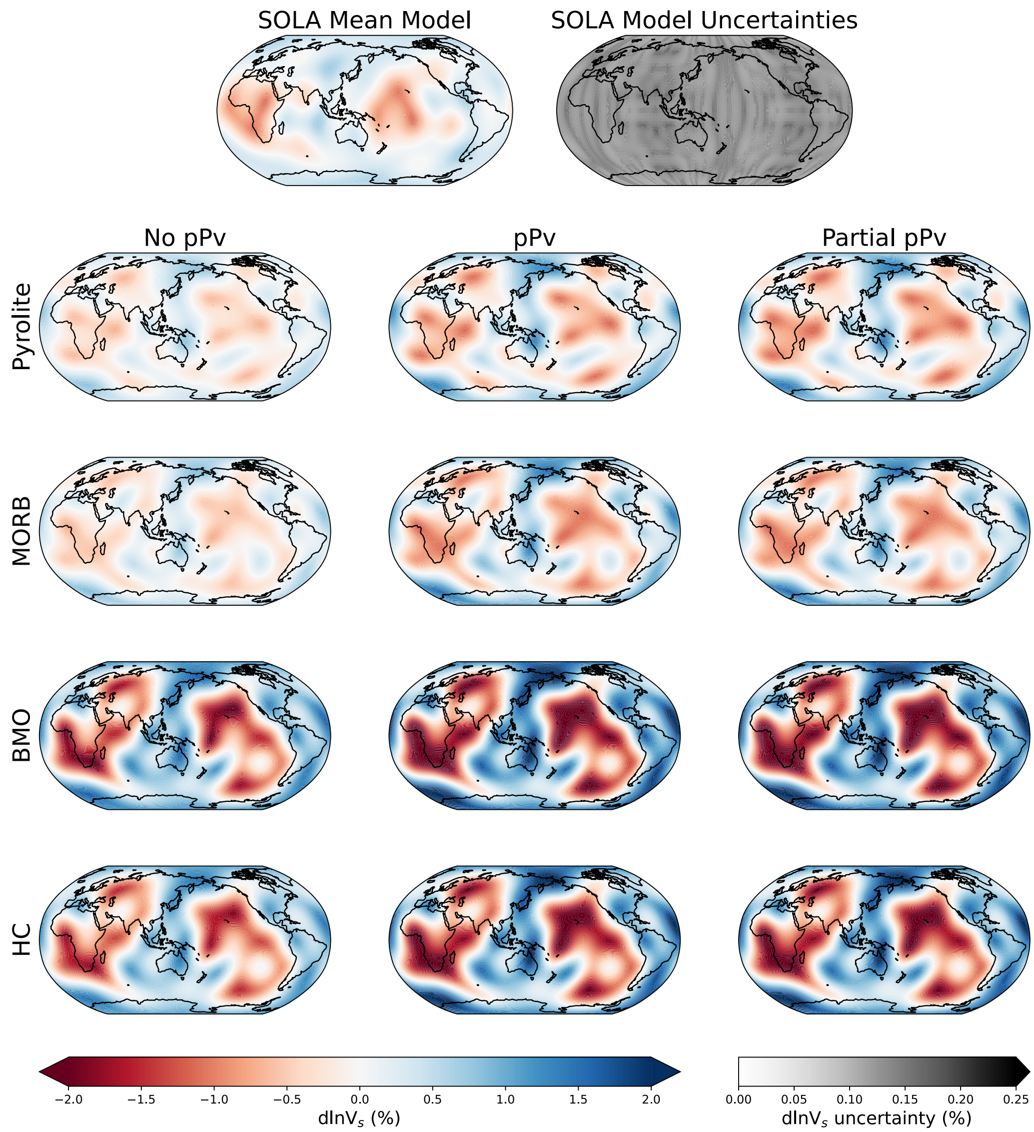

Figure 4: Depth slices for $d \ln V_s$ amplitudes of the filtered synthetic velocity models, organised by post-perovskite (pPv) scenario in columns and LLVP composition in rows. The mean and uncertainty (1σ) of the tomography model of Restelli et al. (2023) in the lowermost mantle are shown on the top. Acronyms for the compositions (row labels) are the same as those in Fig. 2.

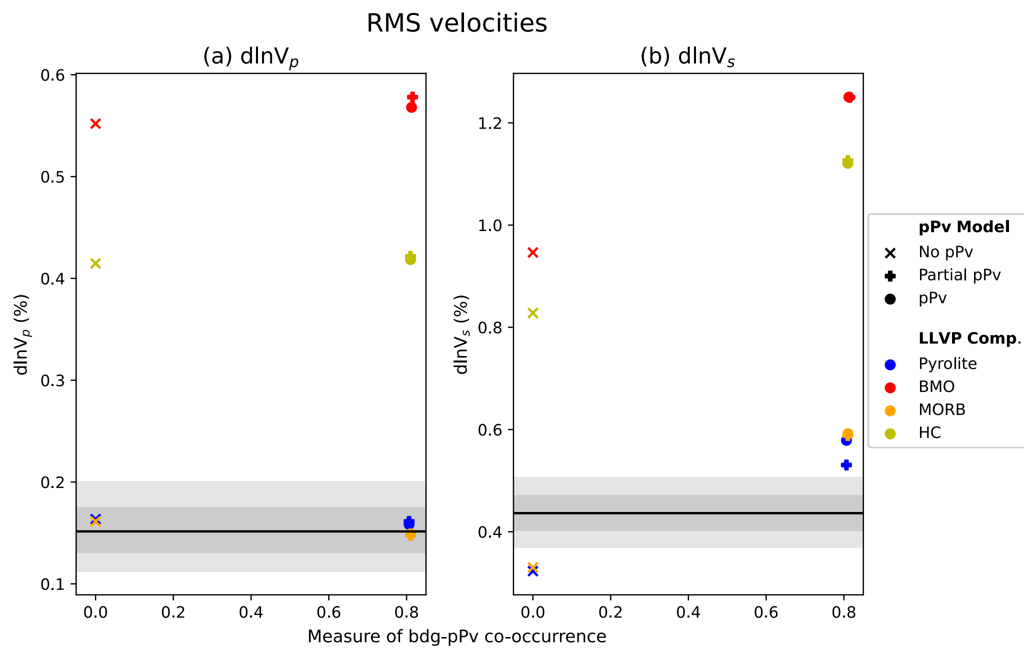

Figure 5: Root mean square of (a) $d\ln V_p$ and (b) $d\ln V_s$ from filtered synthetic velocity models. The colour and symbol of each point represent the LLVP composition and post-perovskite scenario of the synthetic model, respectively (see the figure legend for more details). Black lines and grey shaded regions show the mean and uncertainty of the tomography model of Restelli et al. (2023) respectively, where the darker and lighter shading refers to the region of 1σ and 2σ respectively. The x-axis is a measure of the co-occurrence of bdg-pPv. This measure is calculated by first taking the difference between the maximum and minimum post-perovskite fraction at each depth of the synthetic velocity model. The values of the differences at each depth are then averaged to obtain a single number for the measure of bdg-pPv co-occurrence.

LLVP compositions fit within 1σ of tomographic observations, whereas iron-rich compositions (BMO, red and HC, khaki) have RMS values for $d\ln V_p$ that are at least three times larger than the observed tomographic value. However, none of the models fit the RMS of $d\ln V_s$ within the 2σ uncertainty region of the tomographic observations of Restelli et al. (2023). Nonetheless, models with pyrolite or MORB LLVP compositions have RMS values that are closer to tomographic observations than the iron-rich LLVP compositions, which have RMS values for $d\ln V_s$ that are at least twice as large as the mean value of the tomographic model. In contrast, the difference in RMS values for $d\ln V_s$ between the mean value of the tomographic model and synthetic models with pyrolite and MORB LLVP compositions is no more than 0.2%. Therefore, based on the seismic velocity amplitudes, it is unlikely that the LLVPs are entirely made up of material with a high iron composition.

3.2. Ratios and correlations of velocity anomalies

To better understand the behaviour of the ratios and correlations of velocity variations with depth in the lowermost mantle, we first consider their values in the synthetic velocity models before filtering (Fig. 6), where depth information has not yet been removed by the filtering process (step 4-6 in Fig 1). In Fig. 6, one finds similar shapes across all compositions: "n-shaped arches" in $R_{s/p}$ (top row) and "u-shaped arches" in r_{s-c} (bottom row). $R_{s/p}$ increases sharply between post-perovskite fractions of 0 to around 0.2, then increases very gradually and reaches a peak value between post-perovskite fractions of 0.2 and 0.8, before it decreases sharply back to 2 above a post-perovskite fraction of 0.8. Similar to $R_{s/p}$, there are sharp changes in r_{s-c} at post-perovskite fractions below 0.2 and above 0.8, reaching maximum negative correlation values at intermediate post-perovskite fractions. The main differences in $R_{s/p}$ and r_{s-c} between LLVP compositions are their respective peak values are the steepness of the "arches". Models with pyrolite (Fig 6a) and MORB (Fig 6c) LLVP compositions show relatively symmetric

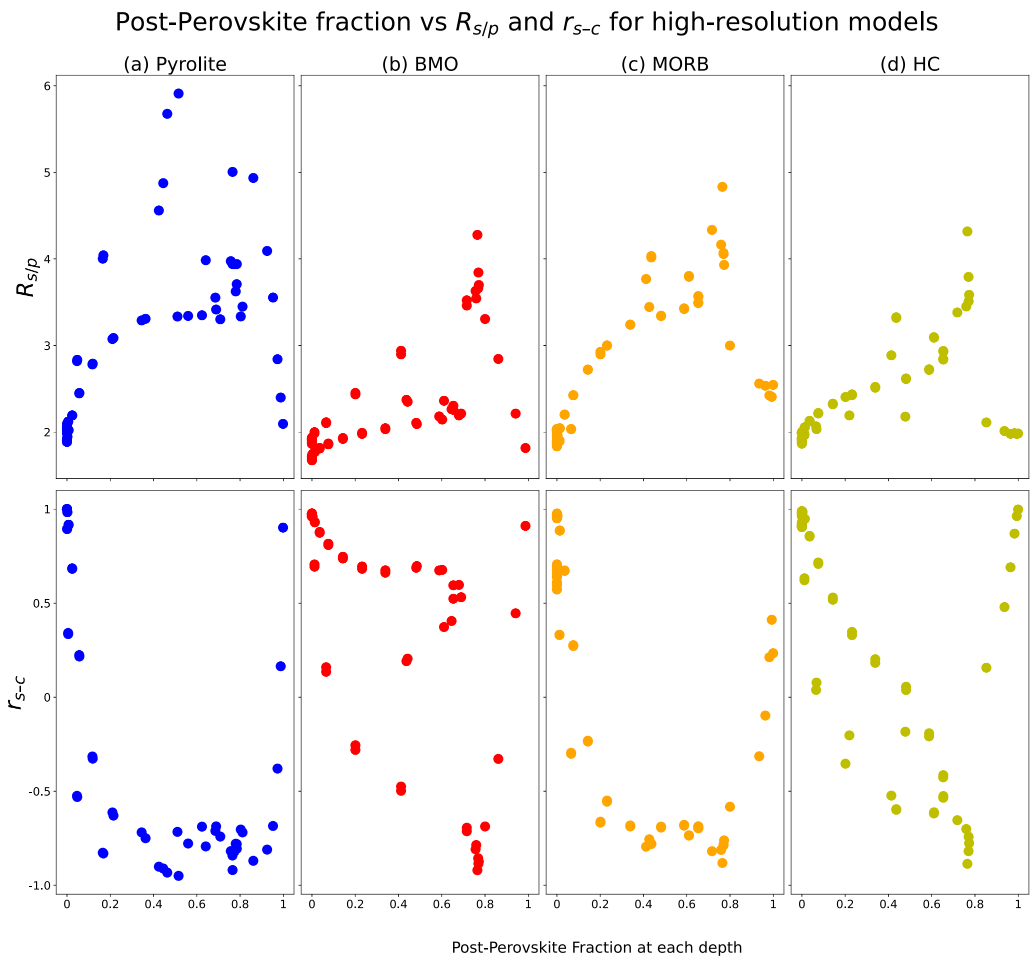

Figure 6: $R_{s/p}$ ($d \ln V_s / d \ln V_p$, top) and r_{s-c} ($d \ln V_s - d \ln V_c$ correlation, bottom) at each depth in synthetic velocity models before filtering, plotted against the average post-perovskite fraction at each depth. Each circle represents an averaged post-perovskite fraction value over a depth layer in the unfiltered models, such that a point with a post-perovskite fraction equal to 0 represents a depth layer with no post-perovskite, and 1 represents a depth layer with no bridgmanite. Each column of subplots corresponds to the LLVP composition used for the specific suite of synthetic velocity models, which is also colour-coded the same as in other plots in the paper for consistency. See Fig. 2 for LLVP composition acronyms.

"arches", reaching peak values of $R_{s/p} > 3.5$ and $r_{s\text{–}c} < 0.6$. In contrast, models with BMO (Fig 6b) and HC (Fig 6d) LLVP compositions show more gradual changes and asymmetric "arches" skewed to the left. The BMO and HC LLVP compositions also have slightly lower peak values, with not many depths having values of $R_{s/p}$ above 2.5 and $r_{s\text{–}c}$ lower than -0.5. Additionally, for all LLVP compositions, $R_{s/p} \approx 2$ and $r_{s\text{–}c} \approx 1$ when the depth average post-perovskite fraction is 0 (depth layer contains no post-perovskite) or 1 (depth layer contains no bridgmanite). This suggests in the absence of tomographic filtering, lowermost mantle signatures of elevated $R_{s/p}$ and $r_{s\text{–}c}$ anti-correlations cannot be explained purely by chemical heterogeneity, but can only be achieved when there is an intermediate post-perovskite fraction (i.e. a co-occurrence) of both bridgmanite and post-perovskite at the same depth.

After applying the resolving kernel to our suite of synthetic models, we obtain our filtered results, where each synthetic model is averaged to one $R_{s/p}$ and one $r_{s\text{–}c}$ value (Fig. 7). All filtered models containing post-perovskite (plus sign and circle symbol) fit within 2σ uncertainty bounds of the observed $R_{s/p}$ in tomography (Fig. 7a). In particular, the models with HC LLVP composition and the model with pyrolite LLVP composition for the "partial-pPv" scenario fit within the 1σ uncertainty. Conversely, all models without post-perovskite (cross sign) have $R_{s/p}$ values that are too low to fit within the 2σ uncertainties of the tomographic observations. Similar patterns are observed in $r_{s\text{–}c}$ (Fig. 7b). Despite none of the synthetic velocity models fitting the 2σ uncertainty of the tomographic model, those without post-perovskite only generate a positive $r_{s\text{–}c}$ and therefore cannot explain the anti-

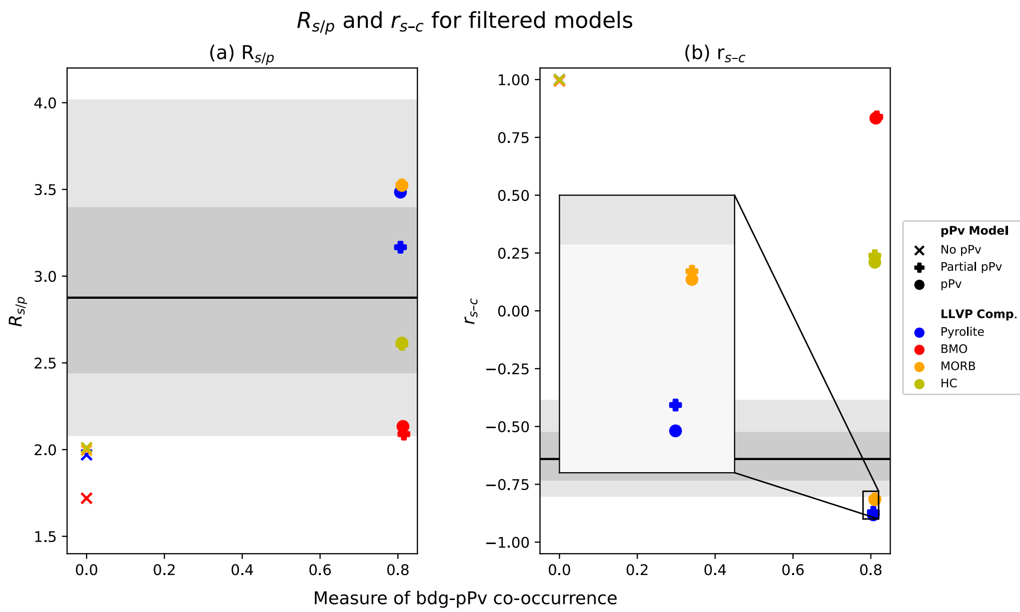

Figure 7: $R_{s/p}$ (left) and r_{s-c} (right) of filtered synthetic velocity models. See Fig. 5 for details of the different symbols and lines.

correlation that is observed in the lowermost mantle. Within the models with post-perovskite, only those with MORB and pyrolite LLVP compositions display negative r_{s-c}. Hence, by excluding synthetic models that do not fit within tomographic uncertainties, our results quantitatively show that models without post-perovskite do not explain both the elevated $R_{s/p}$ and negative r_{s-c} signatures observed in the lowermost mantle.

4. Discussion

Our study quantitatively compares synthetic velocity models of various LLVP structures, compositions and post-perovskite stability scenarios with tomography observations. We show that the ratios and correlations of velocity anomalies can only be explained when bridgmanite and post-perovskite co-occur at depth, without the need for compositional heterogeneity. Our findings are in agreement with Koelemeijer et al. (2018), who explained elevated $R_{s/p}$ and negative $r_{s\text{–}c}$ values in the lowermost mantle by the existence of both bridgmanite and post-perovskite in either a pyrolite or MORB LLVP compositions. Previous synthetic-tomographic comparison studies (e.g. Davies et al., 2012; Koelemeijer et al., 2018) have shown that models containing post-perovskite fit better with tomographic signatures than those without. Our results confirm this statement, as the tomographic uncertainties of Restelli et al. (2023) allow us to conclusively determine that models without post-perovskite do not fit with tomographic observations (Fig. 7). Similar to Koelemeijer et al. (2018), our results additionally show that it is not the existence of post-perovskite, but a co-occurrence of both bridgmanite and post-perovskite at a given depth that explains elevated $R_{s/p}$ and negative $r_{s\text{–}c}$ in the lowermost mantle. If the elevated ratios and anti-correlation were explained purely by the presence of post-perovskite, we would expect to have the highest $R_{s/p}$ and strongest negative $r_{s\text{–}c}$ when the post-perovskite fraction is equal to 1. However, Fig. 6 shows that the strongest negative $r_{s\text{–}c}$ and highest $R_{s/p}$ for all LLVP compositions are present at intermediate post-perovskite fractions between 0.3 to 0.8, where significant amounts of both bridgmanite and post-perovskite are present.

The co-occurrence of bridgmanite and post-perovskite within the same depth happen because of two reasons: (i) a bdg-pPv two-phase region; or (ii) topographic variation of the bdg-pPv phase boundary. A two-phase region typically occurs when there is compositional variation, and one of the compositional end-member transitions to the higher-pressure phase before the other end-member. Because Fe-rich bridgmanite becomes unstable at lower pressures relative to Mg-rich bridgmanite, a mixed-phase assemblage of Fe-rich post-perovskite and Mg-rich bridgmanite can co-exist in equilibrium for pressure and temperature conditions within the two-phase region (Catalli et al., 2009; Mao et al., 2004). Topographic variations of phase transitions with non-zero Clapeyron slope exist when temperature and compositional variations at constant pressures allow both phases to co-occur at the same depth (Styles et al., 2011). A positive Clapeyron slope indicates that post-perovskite will be more stable at colder temperatures and bridgmanite at warmer temperatures at the same pressure (Cobden et al., 2015; Hirose, 2006). Between these two mechanisms for co-occurence, we believe that a two-phase region alone is not enough to explain the increased $R_{s/p}$ and negative r_{s-c} observed in seismic tomography. Even though bridgmanite and post-perovskite exist as separate phases within the two-phase region, the Voigt-Reuss-Hill approximation returns averaged elastic parameters, such that differences in seismic velocities between these two phases are no longer preserved. In contrast, lateral topography variations in a phase transition lead to larger lateral differences relative to a 1-D average, and thus larger RMS velocities (Styles et al., 2011). Because the bdg-pPv phase transition increases V_s by 1-4 %, the radial V_s average increases when bridgmanite transitions to post-perovskite. With an increase in the radial average, the difference in V_s, or $d\ln V_s$, between bridgmanite and the radial average also increases (Fig. 8b). As V_p does not change significantly with the phase transition, $d\ln V_p$ remains relatively constant for an increase in post-perovskite (Fig. 8a), therefore $R_{s/p}$ increases. Similarly, the decrease in V_c due to the phase transition reduces the radial V_c average. This increases $d\ln V_c$, but in the opposite spatial pattern to $d\ln V_s$, hence creating a negative $r_{s\text{-}c}$ (Fig. 8c). Therefore, even if a phase transition has a thick two-phase region, the topography of the phase transition is more important for seismic tomography, where velocity anomalies compared to a radial average are observed (Styles et al., 2011).

On top of that, our study shows that composition alone is insufficient to explain the elevated $R_{s/p}$ and negative $r_{s\text{-}c}$ observed in the lowermost mantle, corroborating findings from Davies et al. (2012), Davies et al. (2015), and Koelemeijer et al. (2018). Fig. 7 shows that the synthetic models of any LLVP composition with no post-perovskite have $R_{s/p}$ of around 2 and $r_{s\text{-}c}$ near 1. These ratios and correlations do not fit within the tomographic observations and uncertainties of Restelli et al. (2023), and they are not markedly different from those associated with thermal effects. Hence, we can concretely disregard the synthetic models with no post-perovskite up to a 2σ confidence level. As such, we confirm that the $R_{s/p}$ and $r_{s\text{-}c}$ are dominantly sensitive to the presence of post-perovskite in the lowermost mantle, and hence should not be used as seismic observations to argue for a compositional heterogeneous mantle (consistent with Davies et al., 2015; Koelemeijer et al., 2018; Tesoniero et al., 2016).

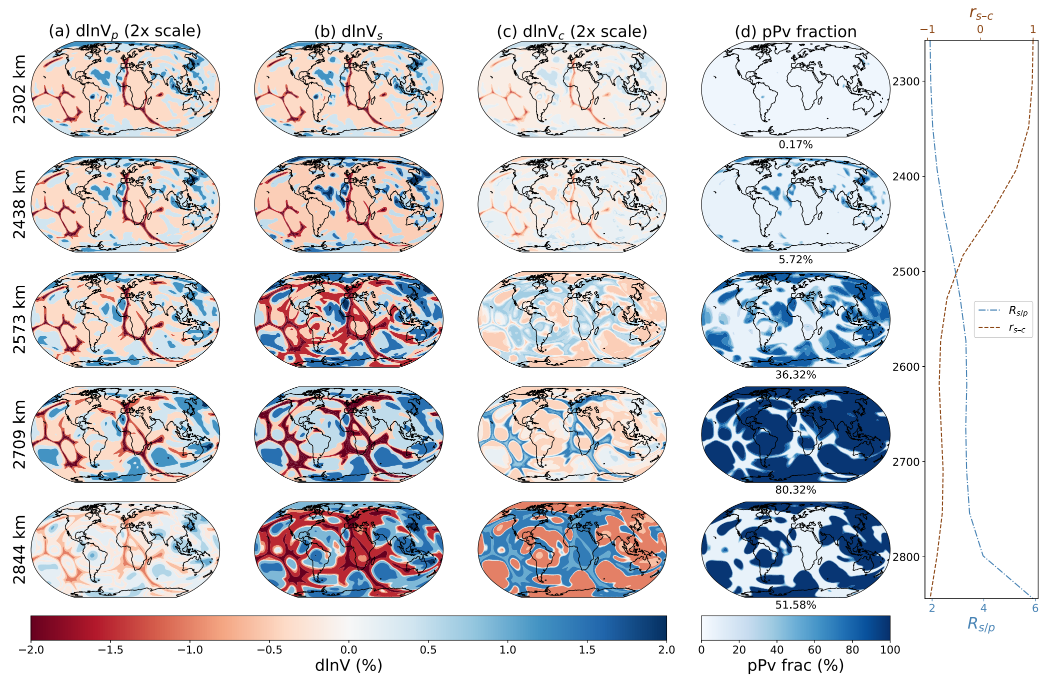

Figure 8: A series of depth slices to illustrate the effect of the co-occurrence of bridgmanite and post-perovskite (pPv) on velocity anomalies, taken from the synthetic model with the "pPv" scenario and a pyrolite composition. Depth slices from left to right: $d\ln V_p$, $d\ln V_s$, $d\ln V_c$, pPv fraction. The amplitudes of $d\ln V_p$ and $d\ln V_c$ are amplified 2x relative to the seismic velocity scale bar (bottom left), so that the two plots have similar colour intensity and patterns when the $R_{s/p} = 2$. The radially averaged ratio $R_{s/p}$ (blue dashdot line) and r_{s-c} (brown dashed line) with depth are shown in the rightmost plot.

Our results, however, do not preclude the possibility of LLVPs as thermo-chemical structures. Even though ratios and correlations of seismic velocity anomalies are mostly sensitive to the bdg-pPv phase transition, other physical parameters, such as density, amplitudes of seismic velocity anomalies, and correlations between density and velocity anomalies, can be used as proxies for LLVP composition (Karato and Karki, 2001; Robson et al., 2021). The values of RMS for $d \ln V_s$ and $r_{s\text{–}c}$ of all our synthetic models do not fit within the uncertainties of the tomographic observations. We believe they are attributed to the following reasons: (i) the elastic parameters calculated from mineral physics are oversensitive to temperature and composition; (ii) the absence of including dynamic effects of the post-perovskite phase transition and (iii) the assumption of the LLVP compositions in this study are oversimplified. To address the first reason regarding the mineralogical model, we conduct additional comparisons with synthetic models calculated by mineralogical model SLB2011 (Stixrude and Lithgow-Bertelloni, 2011). Despite significant differences in the bdg-pPv phase boundary (Fig. S3), we still obtain similar conclusions from models calculated by this mineralogical model: Fe-rich compositions continue to show RMS velocity anomalies that are too large to explain tomographic observations (Fig. S2), and a co-occurrence of bridgmanite and post-perovskite is still required to explain values of elevated $R_{s/p}$ and negative $r_{s\text{–}c}$ in the lowermost mantle (Fig. S4). Expanding on the second reason, post-perovskite is thought to destabilise the thermal boundary layer above the CMB and promote plume formation (Ammann et al., 2010; Hirose, 2006). These dynamic effects should ideally be included, but the exact quantification of these effects remains uncertain, especially when considering anisotropy and slip mechanism of post-perovskite (Cobden et al., 2015; Goryaeva et al., 2016). Furthermore, these effects are unlikely to be visible in our results, given that we only consider depth averages of laterally long-wavelength, present-day tomographic signatures over the lowermost mantle. Third, our study assumes that the entire LLVP contains one type of chemically distinct material because we define the locations of

LLVPs using the compositional field in the geodynamic model of Davies et al. (2012). However, LLVPs could be composed of a mixture or layers of different thermochemical material (Ballmer et al., 2016; Tackley, 2012; Jones et al., 2021). For example, Richards et al. (2023) recently suggested that LLVPs are mostly thermal features that only contain denser thermochemical material in the bottom 200 km. We examine this idea in an additional set of synthetic velocity models where the LLVPs only contain thermochemical material in the bottom 200 kilometers of the mantle. These models have much more comparable amplitudes to the tomography model, such that models of pyrolite and MORB LLVP composition fit within the uncertainties of both $d \ln V_p$ and $d \ln V_s$ RMS values (Fig. S5). However, this idea is not consistent with the geodynamic model, and layered LLVPs should be explored further in geodynamic simulations.

Given that elevated $R_{s/p}$ ratios and $r_{s\text{–}c}$ anti-correlations are both indicators of the co-occurrence of bridgmanite and post-perovskite, we expect these signatures to get stronger when the depth interval of the layer with the co-occurence increases, such that it may be possible to use these signatures to constrain the two-phase region and depth of the bdg-pPv phase transition. However, we cannot constrain these properties in this study as the tomography (Restelli et al., 2023) only offers a depth-averaged image of the lowermost mantle. The thickness of the two-phase region may affect the strength of $R_{s/p}$ and $r_{s\text{–}c}$ after tomographic filtering, but this cannot be constrained given the tomographic uncertainties in Restelli et al. (2023). Similarly, we cannot determine whether a double-crossing of post-perovskite at the base of the mantle occurs, as suggested by previous studies (Hernlund et al., 2005). In our unfiltered results, we see that post-perovskite transitions back to bridgmanite at the base of the mantle due to a steep increase in temperature (Fig. 6). However, this is heavily dependent on the choice of the mineralogical model, as the double-crossing is not observed in synthetic tomograhpic images calculated with the SLB2011 mineralogical model. Future improvements in seismic tomography to obtain better depth resolution with uncertainties will make it possible to better constrain the thickness and depth of the bdg-pPv phase boundary and the existence of the double-crossing.

5. Conclusion

We quantitatively investigate the nature of the LLVPs by comparing a Backus-Gilbert (BG) tomographic model with synthetic velocity models for various LLVP compositions and post-perovskite stability scenarios. The BG model provides robust ratios and correlations of velocity variations derived from nearly equal V_p and V_s resolution, and includes uncertainty quantification that encompasses both data and theoretical errors. By rejecting synthetic models that do not fit within tomographic uncertainties, we show that two groups of models cannot explain tomographic signatures in the lowermost mantle. First, iron-rich compositions result in velocity anomaly amplitudes that are too large to explain tomographic observations. Second, the co-occurrence of bridgmanite and post-perovskite is required to generate the elevated $R_{s/p}$ ratio ($d\ln V_s/d\ln V_p$) and r_{s-c} ($d\ln V_s$-$d\ln V_c$) anticorrelation observed in the lowermost mantle. Our results show that the effects of composition and mineralogy in the lowermost mantle can be separated, with amplitudes of seismic velocity anomalies dominantly affected by composition, and the ratios and correlations mostly linked to phase transitions, confirming that $R_{s/p}$ and r_{s-c} should not be used as arguments for chemical heterogeneity in the lowermost mantle. However, our results do not imply that LLVPs are purely thermal features, and instead encourage further research using other seismic and density observations to better constrain the composition and origin of LLVPs.

CRediT authorship contribution statement

Justin Leung: Conceptualization, Data curation, Funding acquisition, Methodology, Software, Visualization, Writing – original draft, Writing – review & editing. **Andrew M. Walker:** Conceptualization, Methodology, Project administration, Software, Supervision, Writing – review & editing. **Paula Koelemeijer:** Conceptualization, Funding acquisition, Methodology, Software, Supervision, Writing – review & editing. **Federica Restelli:** Data Curation, Writing – review & editing. **D. Rhodri Davies:** Data Curation, Writing – review & editing.

Acknowledgments

J.L. received funding from a NERC DTP Award (NE/S007474/1). J.L. also acknowledges the financial support from SEDI to attend the 18th SEDI Symposium in Great Barrington (2024). P.K. acknowledges financial support from a Royal Society University Research Fellowship (URF\R1\180377).

Data Availability

The Python used for the analysis and figure production in this manuscript can be found online at https://github.com/justinleung4732/tomoproxy. For access to the data used in this study, please contact D.R.D. (rhodri.davies@anu.edu.au) for the geodynamic input fields and P.K. (paula.koelemeijer@earth.ox.ac.uk) for the seismic tomography model.

References

Akbarashrafi, F., Al-Attar, D., Deuss, A., Trampert, J., Valentine, A.P., 2018. Exact free oscillation spectra, splitting functions and the resolvability of Earth's density structure. Geophysical Journal International 213, 58–76. URL: https://academic.oup.com/gji/article/213/1/58/4757069, doi:10.1093/gji/ggx539.

Ammann, M.W., Brodholt, J.P., Wookey, J., Dobson, D.P., 2010. First-principles constraints on diffusion in lower-mantle minerals and a weak D layer. Nature 465, 462–465. URL: https://www.nature.com/articles/nature09052, doi:10.1038/nature09052.

Ballmer, M.D., Schumacher, L., Lekic, V., Thomas, C., Ito, G., 2016. Compositional layering within the large low shear-wave velocity provinces in the lower mantle. Geochem. Geophys. Geosyst. 17, 5056–5077. URL: https://onlinelibrary.wiley.com/doi/10.1002/2016GC006605, doi:10.1002/2016GC006605.

Burke, K., Steinberger, B., Torsvik, T.H., Smethurst, M.A., 2008. Plume Generation Zones at the margins of Large Low Shear Velocity Provinces on the core–mantle boundary. Earth and Planetary Science Letters 265, 49–60. URL: https://linkinghub.elsevier.com/retrieve/pii/S0012821X07006036, doi:10.1016/j.epsl.2007.09.042.

Catalli, K., Shim, S.H., Prakapenka, V., 2009. Thickness and

Clapeyron slope of the post-perovskite boundary. Nature 462, 782–785. URL: `https://www.nature.com/articles/nature08598`, doi:10.1038/nature08598.

Cobden, L., Thomas, C., Trampert, J., 2015. Seismic Detection of Post-perovskite Inside the Earth, in: Khan, A., Deschamps, F. (Eds.), The Earth's Heterogeneous Mantle. Springer International Publishing, Cham, pp. 391–440. doi:10.1007/978-3-319-15627-9_13.

Cottaar, S., Lekic, V., 2016. Morphology of seismically slow lower-mantle structures. Geophysical Journal International 207, 1122–1136. URL: `https://academic.oup.com/gji/article/207/2/1122/2583772`, doi:10.1093/gji/ggw324.

Davies, D., Goes, S., Lau, H., 2015. Thermally dominated deep mantle llsvps: a review. The Earth's Heterogeneous Mantle: A Geophysical, Geodynamical, and Geochemical Perspective , 441–477.

Davies, D.R., Davies, J.H., Bollada, P.C., Hassan, O., Morgan, K., Nithiarasu, P., 2013. A hierarchical mesh refinement technique for global 3-d spherical mantle convection modelling. Geoscientific Model Development 6, 1095–1107.

Davies, D.R., Ghelichkhan, S., Hoggard, M., Valentine, A.P., Richards, F.D., 2023. Observations and models of dynamic topography: Current status and future directions. Dynamics of plate tectonics and mantle convection , 223–269.

Davies, D.R., Goes, S., Davies, J., Schuberth, B., Bunge, H.P., Ritsema, J., 2012. Reconciling dynamic and seismic models of Earth's lower mantle: The dominant role of thermal heterogeneity. Earth and Planetary Science Letters 353-354, 253–269. URL: https://linkinghub.elsevier.com/retrieve/pii/S0012821X1200444X, doi:10.1016/j.epsl.2012.08.016.

Dziewonski, A.M., Anderson, D.L., 1981. Preliminary reference Earth model. Physics of the Earth and Planetary Interiors 25, 297–356. URL: https://www.sciencedirect.com/science/article/pii/0031920181900467, doi:https://doi.org/10.1016/0031-9201(81)90046-7.

Forte, A.M., Simmons, N.A., Grand, S.P., 2015. 1.27 - Constraints on Seismic Models from Other Disciplines - Constraints on 3-D Seismic Models from Global Geodynamic Observables: Implications for the Global Mantle Convective Flow, in: Schubert, G. (Ed.), Treatise on Geophysics (Second Edition). second edition ed.. Elsevier, Oxford, pp. 853–907. URL: https://www.sciencedirect.com/science/article/pii/B9780444538024000282, doi:https://doi.org/10.1016/B978-0-444-53802-4.00028-2.

Garnero, E.J., McNamara, A.K., Shim, S.H., 2016. Continent-sized anomalous zones with low seismic velocity at the base of Earth's mantle. Nature Geosci 9, 481–489. URL: https://www.nature.com/articles/ngeo2733, doi:10.1038/ngeo2733.

Goryaeva, A.M., Carrez, P., Cordier, P., 2016. Low viscosity and high attenuation in MgSiO3 post-perovskite inferred from atomic-scale calculations.

Sci Rep 6, 34771. URL: https://www.nature.com/articles/srep34771, doi:10.1038/srep34771.

Hager, B.H., Clayton, R.W., Richards, M.A., Comer, R.P., Dziewonski, A.M., 1985. Lower mantle heterogeneity, dynamic topography and the geoid. Nature 313, 541–545. URL: https://www.nature.com/articles/313541a0, doi:10.1038/313541a0.

Hernlund, J.W., Thomas, C., Tackley, P.J., 2005. A doubling of the post-perovskite phase boundary and structure of the Earth's lowermost mantle. Nature 434, 882–886. URL: https://www.nature.com/articles/nature03472, doi:10.1038/nature03472.

Hirose, K., 2006. Postperovskite phase transition and its geophysical implications. Rev. Geophys. 44, RG3001. URL: http://doi.wiley.com/10.1029/2005RG000186, doi:10.1029/2005RG000186.

Hirose, K., Takafuji, N., Sata, N., Ohishi, Y., 2005. Phase transition and density of subducted MORB crust in the lower mantle. Earth and Planetary Science Letters 237, 239–251. URL: https://linkinghub.elsevier.com/retrieve/pii/S0012821X0500419X, doi:10.1016/j.epsl.2005.06.035.

Irifune, T., Tsuchiya, T., 2015. 2.03 - Phase Transitions and Mineralogy of the Lower Mantle, in: Schubert, G. (Ed.), Treatise on Geophysics (Second Edition). second edition ed.. Elsevier, Oxford, pp. 33–60. URL:

https://www.sciencedirect.com/science/article/pii/B9780444538024000300, doi:https://doi.org/10.1016/B978-0-444-53802-4.00030-0.

Ishii, M., Tromp, J., 1999. Normal-Mode and Free-Air Gravity Constraints on Lateral Variations in Velocity and Density of Earth's Mantle. Science 285, 1231–1236. URL: https://www.science.org/doi/10.1126/science.285.5431.1231, doi:10.1126/science.285.5431.1231.

Jones, T., Sime, N., Van Keken, P., 2021. Burying earth's primitive mantle in the slab graveyard. Geochemistry, Geophysics, Geosystems 22, e2020GC009396.

Jones, T.D., Maguire, R.R., Van Keken, P.E., Ritsema, J., Koelemeijer, P., 2020. Subducted oceanic crust as the origin of seismically slow lower-mantle structures. Prog Earth Planet Sci 7, 17. URL: https://progearthplanetsci.springeropen.com/articles/10.1186/s40645-020-00327-1, doi:10.1186/s40645-020-00327-1.

Karato, S., Karki, B.B., 2001. Origin of lateral variation of seismic wave velocities and density in the deep mantle. Journal of Geophysical Research: Solid Earth 106, 21771–21783. URL: https://agupubs.onlinelibrary.wiley.com/doi/10.1029/2001JB000214, doi:10.1029/2001JB000214.

Koelemeijer, P., Ritsema, J., Deuss, A., Van Heijst, H.J., 2016. SP12RTS: a degree-12 model of shear- and compressional-wave velocity for Earth's mantle. Geophys. J. Int. 204, 1024–1039. URL:

https://academic.oup.com/gji/article-lookup/doi/10.1093/gji/ggv481, doi:10.1093/gji/ggv481.

Koelemeijer, P., Schuberth, B., Davies, D., Deuss, A., Ritsema, J., 2018. Constraints on the presence of post-perovskite in Earth's lowermost mantle from tomographic-geodynamic model comparisons. Earth and Planetary Science Letters 494, 226–238. URL: https://linkinghub.elsevier.com/retrieve/pii/S0012821X18302656, doi:10.1016/j.epsl.2018.04.056.

Labrosse, S., Hernlund, J.W., Coltice, N., 2007. A crystallizing dense magma ocean at the base of the Earth's mantle. Nature 450, 866–869. URL: https://www.nature.com/articles/nature06355, doi:10.1038/nature06355.

Lee, C.T.A., Luffi, P., Höink, T., Li, J., Dasgupta, R., Hernlund, J., 2010. Upside-down differentiation and generation of a 'primordial' lower mantle. Nature 463, 930–933. URL: https://www.nature.com/articles/nature08824, doi:10.1038/nature08824.

Mao, W.L., Shen, G., Prakapenka, V.B., Meng, Y., Campbell, A.J., Heinz, D.L., Shu, J., Hemley, R.J., Mao, H.k., 2004. Ferromagnesian postperovskite silicates in the D layer of the Earth. Proc. Natl. Acad. Sci. U.S.A. 101, 15867–15869. URL: https://pnas.org/doi/full/10.1073/pnas.0407135101, doi:10.1073/pnas.0407135101.

Masters, G., Gubbins, D., 2003. On the resolution of density within the Earth. Physics of the Earth and Planetary Interiors 140, 159–167. URL: https://linkinghub.elsevier.com/retrieve/pii/S0031920103001705, doi:10.1016/j.pepi.2003.07.008.

Masters, G., Laske, G., Bolton, H., Dziewonski, A., 2000. The Relative Behavior of Shear Velocity, Bulk Sound Speed, and Compressional Velocity in the Mantle: Implications for Chemical and Thermal Structure. Earth's Deep Interior: Mineral Physics and Tomography From the Atomic to the Global Scale 117, 63–87. doi:10.1029/GM117p0063. place: Washington, D. C Publisher: American Geophysical Union.

McNamara, A.K., 2019. A review of large low shear velocity provinces and ultra low velocity zones. Tectonophysics 760, 199–220. URL: https://linkinghub.elsevier.com/retrieve/pii/S0040195118301586, doi:10.1016/j.tecto.2018.04.015.

Moulik, P., Ekström, G., 2016. The relationships between large-scale variations in shear velocity, density, and compressional velocity in the Earth's mantle. JGR Solid Earth 121, 2737–2771. URL: https://agupubs.onlinelibrary.wiley.com/doi/10.1002/2015JB012679, doi:10.1002/2015JB012679.

Murakami, M., Hirose, K., Kawamura, K., Sata, N., Ohishi, Y., 2004. Post-Perovskite Phase Transition in $MgSiO_3$. Science 304, 855–858. URL: https://www.science.org/doi/10.1126/science.1095932, doi:10.1126/science.1095932.

Myhill, R., Cottaar, S., Heister, T., Rose, I., Unterborn, C., Dannberg, J., Gassmoeller, R., 2023. BurnMan – a Python toolkit for planetary geophysics,geochemistry and thermodynamics. JOSS 8, 5389. URL: https://joss.theoj.org/papers/10.21105/joss.05389, doi:10.21105/joss.05389.

Ni, S., Tan, E., Gurnis, M., Helmberger, D., 2002. Sharp Sides to the African Superplume. Science 296, 1850–1852. URL: https://www.science.org/doi/10.1126/science.1070698, doi:10.1126/science.1070698.

Niu, Y., 2018. Origin of the LLSVPs at the base of the mantle is a consequence of plate tectonics – A petrological and geochemical perspective. Geoscience Frontiers 9, 1265–1278. URL: https://linkinghub.elsevier.com/retrieve/pii/S1674987118300847, doi:10.1016/j.gsf.2018.03.005.

Oganov, A.R., Ono, S., 2004. Theoretical and experimental evidence for a post-perovskite phase of MgSiO3 in Earth's D layer. Nature 430, 445–448. URL: https://doi.org/10.1038/nature02701, doi:10.1038/nature02701.

Restelli, F., Zaroli, C., Koelemijer, P., 2023. Robust estimates of the ratio between S- and P-wave velocity anomalies in the Earth's mantle using normal modes. preprint. Physical Sciences and Mathematics. URL: https://eartharxiv.org/repository/view/5933/, doi:10.31223/X5539D.

Richards, F.D., Hoggard, M.J., Ghelichkhan, S., Koelemeijer, P., Lau, H.C., 2023. Geodynamic, geodetic, and seismic constraints favour deflated and dense-cored LLVPs. Earth and Planetary Science Letters 602, 117964. URL: https://linkinghub.elsevier.com/retrieve/pii/S0012821X22006008, doi:10.1016/j.epsl.2022.117964.

Ritsema, J., Deuss, A., Van Heijst, H.J., Woodhouse, J.H., 2011. S40RTS: a degree-40 shear-velocity model for the mantle from new Rayleigh wave dispersion, teleseismic traveltime and normal-mode splitting function measurements: S40RTS. Geophysical Journal International 184, 1223–1236. URL: https://academic.oup.com/gji/article-lookup/doi/10.1111/j.1365-246X.2010.04884.x doi:10.1111/j.1365-246X.2010.04884.x.

Ritsema, J., Van Heijst, H.J., 2002. Constraints on the correlation of *P* - and *S* -wave velocity heterogeneity in the mantle from *P* , *PP* , *PPP* and *PKP* ab traveltimes. Geophysical Journal International 149, 482–489. URL: https://academic.oup.com/gji/article/149/2/482/728317, doi:10.1046/j.1365-246X.2002.01631.x.

Robson, A., Lau, H.C.P., Koelemeijer, P., Romanowicz, B., 2021. An analysis of core–mantle boundary Stoneley mode sensitivity and sources of uncertainty. Geophysical Journal International 228, 1962–1974. URL: https://academic.oup.com/gji/article/228/3/1962/6413994, doi:10.1093/gji/ggab448.

Schubert, G., Masters, G., Olson, P., Tackley, P., 2004.

Superplumes or plume clusters? Physics of the Earth and Planetary Interiors 146, 147–162. URL: https://linkinghub.elsevier.com/retrieve/pii/S0031920104001128, doi:10.1016/j.pepi.2003.09.025.

Schuberth, B.S.A., Bunge, H., Ritsema, J., 2009a. Tomographic filtering of high-resolution mantle circulation models: Can seismic heterogeneity be explained by temperature alone? Geochem Geophys Geosyst 10, 2009GC002401. URL: https://agupubs.onlinelibrary.wiley.com/doi/10.1029/2009GC002401, doi:10.1029/2009GC002401.

Schuberth, B.S.A., Bunge, H., Steinle-Neumann, G., Moder, C., Oeser, J., 2009b. Thermal versus elastic heterogeneity in high-resolution mantle circulation models with pyrolite composition: High plume excess temperatures in the lowermost mantle. Geochem Geophys Geosyst 10, 2008GC002235. URL: https://agupubs.onlinelibrary.wiley.com/doi/10.1029/2008GC002235, doi:10.1029/2008GC002235.

Stampfli, G., Borel, G., 2002. A plate tectonic model for the Paleozoic and Mesozoic constrained by dynamic plate boundaries and restored synthetic oceanic isochrons. Earth and Planetary Science Letters 196, 17–33. URL: https://linkinghub.elsevier.com/retrieve/pii/S0012821X0100588X, doi:10.1016/S0012-821X(01)00588-X.

Stampfli, G.M., Hochard, C., 2009. Plate tectonics of the Alpine realm. SP 327, 89–111. URL:

https://www.lyellcollection.org/doi/10.1144/SP327.6, doi:10.1144/SP327.6.

Stixrude, L., Lithgow-Bertelloni, C., 2011. Thermodynamics of mantle minerals - II. Phase equilibria. Geophysical Journal International 184, 1180–1213. URL: https://academic.oup.com/gji/article/184/3/1180/625783, doi:10.1111/j.1365-246X.2010.04890.x.

Stixrude, L., Lithgow-Bertelloni, C., 2021. Thermal expansivity, heat capacity and bulk modulus of the mantle. Geophysical Journal International 228, 1119–1149. URL: https://academic.oup.com/gji/article/228/2/1119/6375416, doi:10.1093/gji/ggab394.

Styles, E., Davies, D.R., Goes, S., 2011. Mapping spherical seismic into physical structure: biases from 3-D phase-transition and thermal boundary-layer heterogeneity: 3-D biases in 1-D seismic velocities. Geophysical Journal International 184, 1371–1378. URL: https://academic.oup.com/gji/article-lookup/doi/10.1111/j.1365-246X.2010.04914.x doi:10.1111/j.1365-246X.2010.04914.x.

Su, W.j., Dziewonski, A.M., 1997. Simultaneous inversion for 3-D variations in shear and bulk velocity in the mantle. Physics of the Earth and Planetary Interiors 100, 135–156. URL: https://linkinghub.elsevier.com/retrieve/pii/S0031920196032360, doi:10.1016/S0031-9201(96)03236-0.

Tackley, P.J., 2012. Dynamics and evolution of the deep mantle resulting from thermal, chemical, phase and melting effects. Earth-Science Reviews 110, 1–25. URL: https://linkinghub.elsevier.com/retrieve/pii/S0012825211001486, doi:10.1016/j.earscirev.2011.10.001.

Tarduno, J.A., Watkeys, M.K., Huffman, T.N., Cottrell, R.D., Blackman, E.G., Wendt, A., Scribner, C.A., Wagner, C.L., 2015. Antiquity of the South Atlantic Anomaly and evidence for top-down control on the geodynamo. Nat Commun 6, 7865. URL: https://www.nature.com/articles/ncomms8865, doi:10.1038/ncomms8865.

Tesoniero, A., Cammarano, F., Boschi, L., 2016. StoP heterogeneity ratio in the lower mantle and thermo-chemical implications. Geochem Geophys Geosyst 17, 2522–2538. URL: https://agupubs.onlinelibrary.wiley.com/doi/10.1002/2016GC006293, doi:10.1002/2016GC006293.

Thorne, M.S., Garnero, E.J., Grand, S.P., 2004. Geographic correlation between hot spots and deep mantle lateral shear-wave velocity gradients. Physics of the Earth and Planetary Interiors 146, 47–63. URL: https://linkinghub.elsevier.com/retrieve/pii/S003192010400113X, doi:10.1016/j.pepi.2003.09.026.

Tolstikhin, I., Hofmann, A.W., 2005. Early crust on top of the Earth's core. Physics of the Earth and Planetary Interiors 148, 109–130. URL:

https://linkinghub.elsevier.com/retrieve/pii/S0031920104002961, doi:10.1016/j.pepi.2004.05.011.

Trampert, J., Deschamps, F., Resovsky, J., Yuen, D., 2004. Probabilistic Tomography Maps Chemical Heterogeneities Throughout the Lower Mantle. Science 306, 853–856. URL: https://www.science.org/doi/10.1126/science.1101996, doi:10.1126/science.1101996.

Trautner, V.E., Stackhouse, S., Turner, A.R., Koelemeijer, P., Davies, D.R., Méndez, A.S.J., Satta, N., Kurnosov, A., Liermann, H.P., Marquardt, H., 2023. Compressibility of ferropericlase at high-temperature: Evidence for the iron spin crossover in seismic tomography. Earth and Planetary Science Letters 618, 118296. URL: https://linkinghub.elsevier.com/retrieve/pii/S0012821X23003096, doi:10.1016/j.epsl.2023.118296.

Tsuchiya, T., Tsuchiya, J., Umemoto, K., Wentzcovitch, R.M., 2004. Elasticity of post-perovskite $MgSiO_3$. Geophysical Research Letters 31, 2004GL020278. URL: https://agupubs.onlinelibrary.wiley.com/doi/10.1029/2004GL020278, doi:10.1029/2004GL020278.

Ward, J., Nowacki, A., Rost, S., 2020. Lateral Velocity Gradients in the African Lower Mantle Inferred From Slowness Space Observations of Multipathing. Geochem Geophys Geosyst 21, e2020GC009025. URL: https://agupubs.onlinelibrary.wiley.com/doi/10.1029/2020GC009025, doi:10.1029/2020GC009025.

Zaroli, C., 2016. Global seismic tomography using Backus–Gilbert inversion. Geophys. J. Int. 207, 876–888. URL: https://academic.oup.com/gji/article-lookup/doi/10.1093/gji/ggw315, doi:10.1093/gji/ggw315.